

---

# Load-bearing capacity of welded hollow sphere joints with trapezoidal ribs under combined axial compression and bending moment

Tingting Shu\*, Xian Xu

\*Department of Civil Engineering, Zhejiang University  
Hangzhou, China  
12112008@zju.edu.cn

## Abstract

Welded hollow spherical joints (WHSJs) are prevalent in spatial reticulated structures throughout China. Adding external trapezoidal ribs is an effective strategy for enhancing strength of WHSJ. These joints often bear not just axial forces but also bending moments, such as in single-layer reticulated shells and suspended-dome structures. Eccentric compression is employed to implement the combination of axial compression and bending moment. In this paper, experimental and numerical studies are conducted to investigate the static behavior of WHSJ reinforced with external trapezoidal ribs subjected to eccentric compression. Experiments are conducted on 4 specimens, focusing on the influence of load eccentricity and angle, to reveal the failure mechanism, load-bearing capacity and strain development. It is found that the load-bearing capacity decreases as the load eccentricity increases, and strength failure occurred for the specimens. Subsequently, a refined finite element model is developed and calibrated against the experimental results. The calibrated model is served to carry out parametric study on the load-bearing capacities of the reinforced WHSJ. The lower envelope method is employed to propose a conservative estimation of the load-bearing capacities of WHSJ with trapezoidal ribs under both axial compression and bending moment.

**Keywords:** welded hollow spherical joints, external rib, failure mechanism, load-bearing capacity, design formula.

## 1. Introduction

Welded hollow spherical joints (WHSJs) are widely used in spatial reticulated structures for their reliability and versatility. Incorporating internal ribs is a prevalent strategy to enhance the strength of WHSJ during the design stage. Recently, the application of external ribs has gained increasing interest to strengthen a joint post-construction [1]. WHSJ in single-layer reticulated shells are subjected to both axial force and bending moment, whereas those in double-layer reticulated shells are primarily under axial force.

Over the past few decades, extensive studies have been conducted to address the failure mechanism and strength of WHSJ under axial force. For WHSJ without external ribs under combined axial force and bending moment, Dong et al. [2] established that the correlation of axial compression and bending moment is independent of the hollow sphere's diameter and thickness, as well as the steel tube's diameter, based on theoretical analysis. This finding is consistent across WHSJ with rectangular [3] and square steel tubes [4]. Consequently, the formula for the load-bearing capacities of WHSJ under combined axial force and bending moment can be established based on those under axial force by incorporating a correction coefficient, to account for the effect of the bending moment.

For WHSJ reinforced with external ribs, Guo et al. [5] examined the axial performance of WHSJ with unidirectional annular ribs, and proposed design formulas for their tensile and compressive capacities.

On the other hand, the reinforcement effect of external ribs on the damaged WHSJs are elucidated, considering the loading history of the unreinforced WHSJs and the welding heat induced by the external ribs [6]. Xu et al. [1] and Shu et al. [7] experimentally and numerically investigated the performance of WHSJs reinforced with external trapezoidal and triangular ribs under axial compression and formulas for the axial compressive capacity of them are proposed. Besides, axial compressive performance of WHSJs reinforced with both internal and external ribs is also elucidated [8]. However, to the best of authors' knowledge, limited studies have been reported on the static performance of WHSJs with external ribs under combined axial load and bending moment.

This paper carries out an experimental and numerical study on the static performance of WHSJs reinforced with external trapezoidal ribs under combined axial compression and bending moment. It is structured as follows: Section 2 proposes the form of the formula to calculate the load-bearing capacity of the reinforced WHSJs. Section 3 presents the details of the experiment on 4 full-scale specimens. The experimental results are presented and discussed in Section 4. In Section 5, the reinforced WHSJs are parametrically studied using a FE model calibrated by the experimental results, and a practical formula for the load-bearing capacity of the reinforced WHSJs proposed based on the numerical results. Finally, Section 6 concludes the paper.

## 2. Formula proposal

Eccentric compression is adopted in this study to conservatively evaluate the bearing capacity of the reinforced WHSJs subjected to both axial force and bending moment. Figure 1 illustrates the geometry and notation for the reinforced WHSJs.  $h$  is the height of the external rib, and  $h_1$  is the projection of rib's length along the hollow sphere in the vertical direction, and  $h_1 = h$ , as shown in Figure 1(b). The ribs are evenly spaced around the circumference of the steel tubes, with an equal number of ribs connected to both the upper and lower tubes. Furthermore, the notation  $n$  represents the number of external ribs attached to a single steel tube.

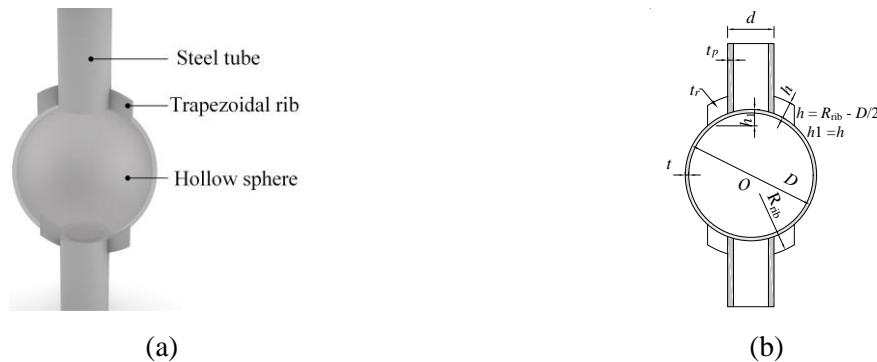
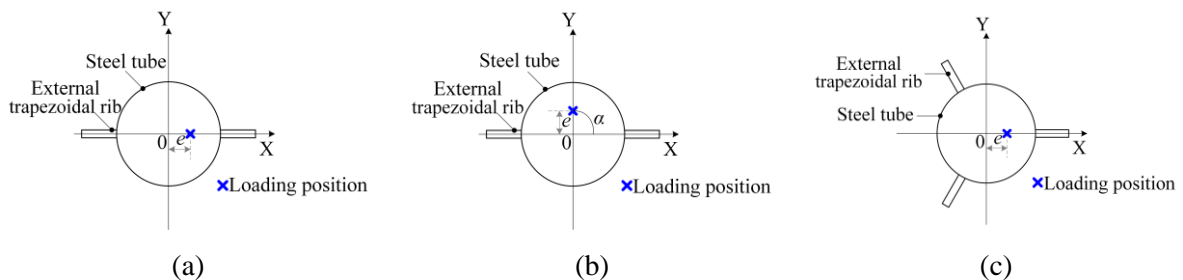


Figure 1: WHSJs with external trapezoidal ribs: (a) Configuration; (b) Geometry

Figure 2 provides a top view schematic of the reinforced WHSJs with varying numbers of external ribs under different loading scenarios, with the load oriented in the positive direction of the X-axis. The load angle,  $\alpha$ , measures the degree from the positive direction of the X-axis to the line formed by the load location and the coordinate origin, while the load eccentricity,  $e$ , defines the distance from the load location to the steel tube's axis.



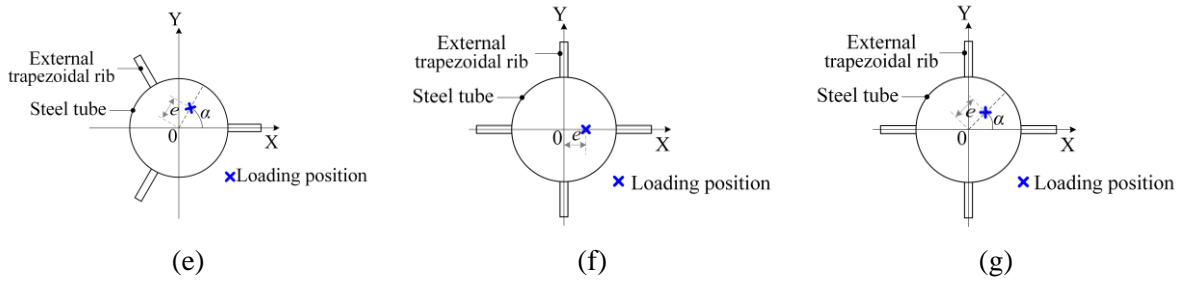


Figure 2: Types of eccentric load: (a)  $n = 2, \alpha = 0^\circ$ ; (b)  $n = 2, \alpha = 90^\circ$ ; (c)  $n = 3, \alpha = 0^\circ$ ; (d)  $n = 3, \alpha = 60^\circ$ ; (e)  $n = 4, \alpha = 0^\circ$ ; (f)  $n = 4, \alpha = 45^\circ$

Thus, the bending moment  $M$  applied on the joints can be calculated as

$$M = Ne \quad (1)$$

where  $N$  denotes eccentric compression.

To examine the impact of the bending moment on the load-bearing capacity of the reinforced WHSJs, Influence coefficients of axial compressive strength  $\eta_N$ , and of pure bending strength  $\eta_M$  are introduced, and calculated as

$$\eta_N = \frac{N_{R, M}}{N_{R, r}} \quad (2)$$

$$\eta_M = \frac{M_{R, M}}{M_{R, r}} \quad (3)$$

where  $N_{R, M}$  and  $M_{R, M}$  represent the axial force and bending moment of the reinforced WHSJs under eccentric compression, respectively.  $N_{R, r}$  and  $M_{R, r}$  denote the axial compressive strength and pure bending strength of the reinforced WHSJs, respectively.

The preliminary analysis though numerical simulation reveals that the values of  $\eta_N$  and  $\eta_M$  are concerned with the load eccentricity  $e$  and angle  $\alpha$  of the eccentric compression, and the number of the external ribs  $n$ .

Given that the joints of spatial reticulated structure members are primarily subjected to axial force, and the load-bearing capacity  $N_R$  provided in China Technical Specification for Space Frame Structures [9] is based on axial force, and calculated as

$$N_R = \eta_0 \left( 0.29 + 0.54 \frac{d}{D} \right) \pi t d f \quad (4)$$

where  $\eta_0 = 1.0$  for  $D \leq 500$  mm, and  $\eta_0 = 0.9$  for  $500 \text{ mm} \leq D \leq 900$  mm; and  $f$  is the design strength of the steel material.

The axial compressive strength  $N_{R, r}$  is detailed in the authors' previous studies [1, 7], and calculated as

$$N_{R, r} = \left( 1.0 + 0.2n \frac{t_r h}{t d} \right) N_R \quad (5)$$

Thus, the calculation formula of the reinforced WHSJs under both axial compression and bending moment is accordingly established based on axial force, and Eq. (2) can be rewritten as

$$N_{R, M} = \eta_N N_{R, r} \quad (6)$$

Based on preliminary analysis, the relationship of  $\eta_N$  and the relevant parameters (number of the external ribs  $n$ , load eccentricity  $e$ , and load angle  $\alpha$ ) needs to be established to determine the load-bearing capacity of the reinforced WHSJs under eccentric compression.

### 3. Experimental program

#### 3.1. Test specimens

Four full-scale specimens are designed to investigate the influence of load eccentricity  $e$  and load angle  $\alpha$  on the static performance of the reinforced WHSJ. Table 1 details the dimensions and loading scenarios, with Figure 1 showing the geometrical descriptions. Furthermore,  $e'$  is the actual load eccentricity measured during the test, which is also documented in Table 1.

All designed specimens share the same dimensions, except for the variables under study. The hollow sphere features an outer diameter ( $D$ ) of 400 mm and a thickness ( $t$ ) of 12 mm. The steel tube has a diameter ( $d$ ) of 159 mm, a thickness ( $t_p$ ) of 20 mm (thicker than typically paired with this hollow sphere, to prevent tube failure before the sphere), and a length ( $h_p$ ) of 280 mm. The external trapezoidal ribs have a thickness ( $t_r$ ) of 12 mm and a height ( $h$ ) of 53 mm. To enhance the repeatability of the test, two specimens are manufactured for each specimen subjected to eccentric compression.

Table 1: Dimensions and load scenarios of specimens

Specimen numbers	External trapezoidal ribs						Numbers of specimens
	$t_r$ (mm)	$h$ (mm)	$n$	$e$ (mm)	$e'$ (mm)	$\alpha$ (deg.)	
S1-n4-e0	12	53	4	0	5	0	1
S2-n4-e40			4	40	35	0	2
S3-n4-e200			4	200	190	0	2
S4-n4-e40- $\alpha$ 45			4	40	40	45	2

#### 3.2. Materials

Uniaxial tensile tests are conducted on three coupons to assess the material properties of the steel in the hollow spheres, in accordance with Chinese specifications [10], as illustrated in Figure 3. The stress-strain curves obtained from the tests are depicted in Figure 4, where the constitutive model for hot-rolled steels proposed by Yun et al. [11] is employed to describe the stress-strain behavior, and is depicted as the blue curve in Figure 4. Table 2 summarizes the average values of the measured material properties from the test results.

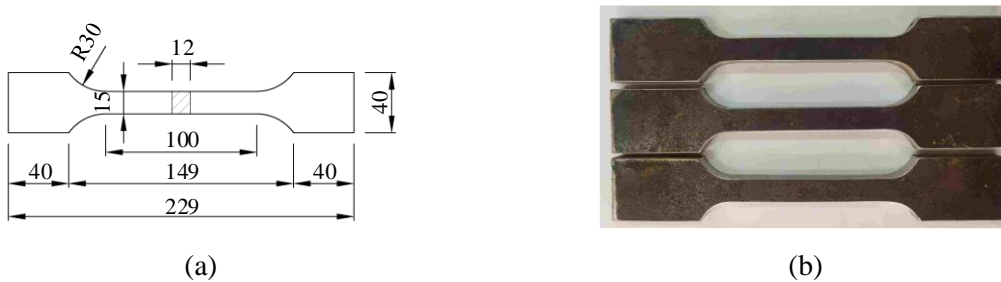


Figure 3: Coupons of tensile test: (a) geometry; (b) physical

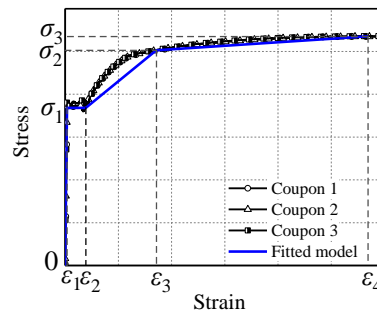


Figure 4: Stress-strain response of test coupons

Table 2: Material properties of steel

$t_c$ (mm)	$E$ (MPa)	$\sigma_1$ (MPa)	$\sigma_2$ (MPa)	$\sigma_3$ (MPa)	$\epsilon_1$ (%)	$\epsilon_2$ (%)	$\epsilon_3$ (%)	$\epsilon_4$ (%)
11.74	209600	368	502	535	0.176	1.94	8.57	28.46

### 3.3. Measurement plan

Two Linear variable displacement transducers (LVDTs) are deployed on the top plate of the specimen to record its vertical displacement. To capture strain variations of the specimens under load, strain gauges and rosettes are employed. Four strain gauges are uniformly arranged around each steel tube in the circular direction, while five strain rosettes are grouped and distributed on the same meridian of the hollow sphere. The arrangement of LVDTs, strain gauges and rosettes for the specimens are illustrated in Figure 5. Displacement and strain variation of each specimen are monitored during the whole loading process, and load readings are tracked using the force sensor integrated into the testing equipment.

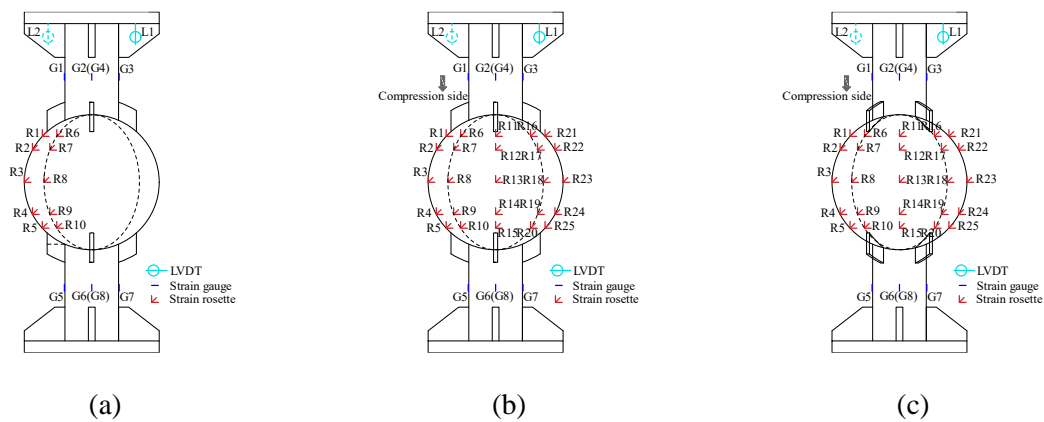


Figure 5: Strain and displacement sensors arrangement: (a) S1; (b) S2-S3; (c) S4

### 3.3. Loading setup and procedure

The experimental setup and schematic sketch for the specimens under eccentric compression are shown in Figure 6. An electrohydraulic servo machine with a maximum capacity of 10,000 kN is employed to apply the vertical eccentric load. To simulate pin-ended boundary conditions for the specimens, the setup combines rolling support with a long arc-shaped grooved plate. This combination removes rotational restraint in the eccentric direction of load, while preventing rotation in the perpendicular direction. The load eccentricity is the distance between the center of the groove and the axis of the steel tube. Prior to formal loading, 20% of the ultimate strength predicted by numerical analysis is applied and maintained for 5 minutes, to eliminate any contact gaps and check the effectiveness of loading and measuring equipment. The test follows a displacement-controlled protocol, starting with a loading rate of 0.2 mm/min, and accelerating to 0.35 mm/min after the load-displacement curve exceeds the peak point. Loading stops when the reaction force of the specimens drops to 80% of its peak strength.

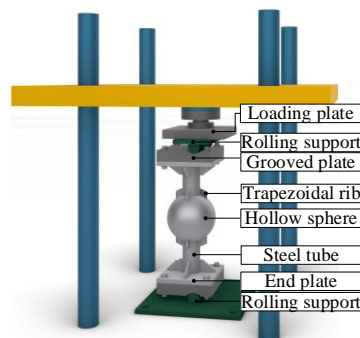


Figure 6: Test setup

## 4. Experimental results and discussion

### 4.1. Failure mode

Figure 7 presents the characteristic failure modes for specimens with 4 external ribs under compression. The deformation is primarily localized at the junction of the hollow sphere, steel tube, and external ribs. Specimen S1, subjected to axial compression, exhibits a uniform downward deformation, accompanied by a noticeable indentation where the hollow sphere interfaces with the edge of the external ribs (Figure 7(a)). Specimens S2 to S4 under eccentric compression display significant lateral deflection, with specimen S3 experiences a larger load eccentricity ( $e = 200$  mm), exhibits more pronounced deformation (Figure 7(b)-(d)).

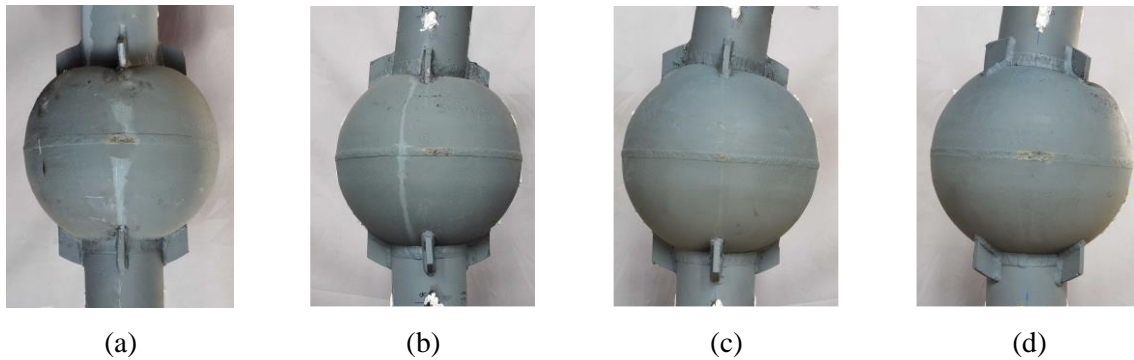


Figure 7: Failure mode of the tested specimens under eccentric compression:  
(a) S1- $n4-e0$ ; (b) S2- $n4-e40$ ; (c) S3- $n4-e200$ ; (d) S4- $n4-e40-\alpha45$

### 4.2. Load-displacement response

Figure 8 presents the load-displacement responses of the specimens under eccentric compression. The “Farthest point method” is utilized to identify the yield point within these responses, denoted by a blue dot in Figure 8, with the yield strength corresponds to the value on the Y-axis. The ultimate strength is indicated by the peak point, signified by a red dot. The yield and ultimate strengths derived from the tests for each specimen are listed in Table 3. A comparison of the results for specimens S1-S3 alongside their corresponding load eccentricities from Table 1, reveals that both yield and ultimate strengths decrease as load eccentricity increases. Additionally, comparing specimens S2 and S4 shows that the strength decreases with an increase in the load angle.

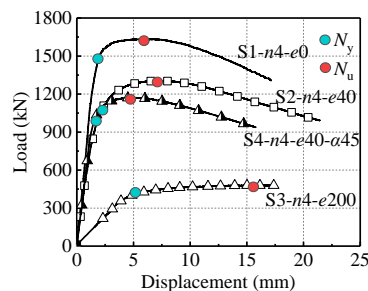


Figure 8: Load-displacement response

Table 3: Strength of tested specimens

Specimen numbers	Test results		Influence coefficient of axial compressive strength $\eta_N$
	$N_y$ (kN)	$N_u$ (kN)	
S1- $n4-e0$	1482	1633	1.0
S2- $n4-e40$	1077	1304	0.73
S3- $n4-e200$	404	480	0.27
S4- $n4-e40-\alpha45$	993	1171	0.67



### 4.3. Strain development

The load-strain responses of specimen S3-*n4-e200* are illustrated in Figure 9, to explore the strain development of the reinforced WHSJs under eccentric compression before reaching ultimate strength. When the specimen reaches the ultimate strength ( $N_u$ ), all of the measuring points close to the conjunction between the steel tube and hollow sphere (R5, R15, R20, and R25) exceed the yield threshold, strength failure occurred. Figure 9(f) illustrates the load-strain responses of the upper and lower steel tubes, the similarity of strains at corresponding positions on both steel tubes validates that the boundary conditions at both ends of the specimen are consistent with a hinged connection. Both the tubes are in the elastic phase throughout the entire loading process suggests that the failure of the specimen initiated in the hollow sphere.

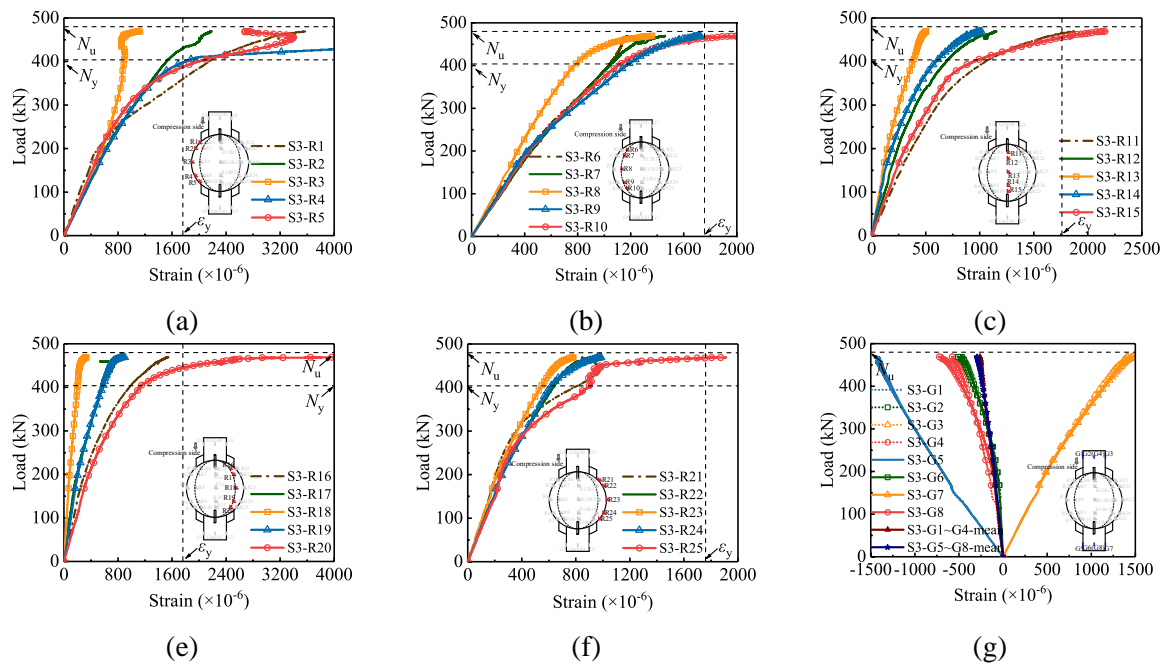


Figure 9: Load-strain response of specimen S3-*n4-e200*: (a) R1~R5; (b) R6~R10; (c) R11~R15; (d) R16~R20; (e) R21~R25; (f) G1~G8

## 5. Numerical simulation

### 5.1. Finite element model

The tested reinforced WHSJs are modeled using ANSYS [12], to generate a computational finite-element model to evaluate their static response. The model, which incorporates geometric nonlinearity and user-defined material constitutive relationships (referenced in Figure 4 and Table 2), employs the Solid 45 element for constructing the specimens. Reference nodes are established on the end faces of both the upper and lower steel tubes, aligned with the actual load eccentricity and angle. The experimentally measured load eccentricity ( $e'$ ) listed in Table 1 is applied to the model. All end-face nodes of the steel tubes are rigidly coupled to their corresponding reference node using the MPC 184 element in ANSYS. To simulate the physical boundary conditions, the lower reference node is restrained in all three directions, while the upper reference node is restrained in the transverse directions, and vertical displacements are applied as recorded in the experiment, as illustrated in Figure 10. The Newton-Raphson method is used to perform the static analysis.

The numerical simulations of specimen S3-*n4-e200*, presenting the equivalent stress contours and deformation, are illustrated in Figure 11. The deformation obtained from the numerical simulation closely align with the experimental results depicted in Figure 7. Figure 12 displays the load-displacement responses from the experiments and numerical simulations, the comparison between them demonstrates a strong similarity.

Consequently, the developed FE model is capable of simulating the static performance of the reinforced WHSJ under eccentric compression.

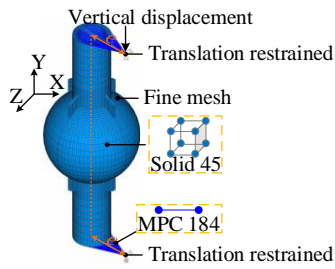


Figure 10: Loading, boundary and mesh illustration for reinforced WHSJ

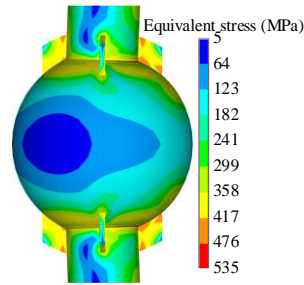


Figure 11: Equivalent stress distribution and deformation from numerical simulation

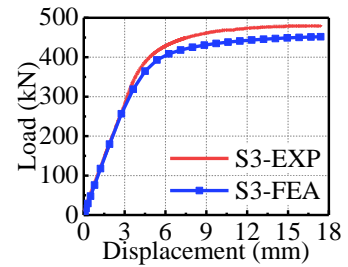


Figure 12: Comparison of load-displacement response between test and numerical simulation

## 5.2. Parametric study

The calibrated model of the reinforced WHSJ is employed, to explore the effect of the relevant parameters (i.e., load eccentricity  $e$ , load angle  $\alpha$ , and number of external trapezoidal ribs  $n$ ) on the influence coefficient of axial compressive strength  $\eta_N$ . To standardize the load eccentricity  $e$  for different steel tubes, the eccentricity ratio  $c$  is introduced, and calculated as follows:

$$c = \frac{e}{d/2} \quad (7)$$

$$c = \frac{2M}{Nd} \quad (8)$$

The parametric combinations are summarized in Table 4. A total of 90 numerical simulations are developed to investigate the static response of reinforced WHSJ under eccentric compression.

Table 4: Parametric combination

$D$ (mm)	$t$ (mm)	$d$ (mm)	$t_r$ (mm)	$h$ (mm)	$n$	$\alpha$ (deg.)	$c$	$e$ (mm)
300	8	114	8	38	2	0, 90	0, 2, 4	0, 114, 228
					3	0, 60		
					4	0, 45		
450	14	168	14	56	2	0, 90		0, 168, 336
					3	0, 60		
					4	0, 45		
600	18	233	18	75	2	0, 90		0, 233, 466
					3	0, 60		
					4	0, 45		
750	25	299	25	94	2	0, 90	0, 299, 598	
					3	0, 60		
					4	0, 45		
900	25	335	25	113	2	0, 90	0, 335, 670	
					3	0, 60		
					4	0, 45		

$D = 600$  mm,  $n = 2$ ,  $c = 2$  and  $\alpha = 0$  are adopted herein to demonstrate the effect of relevant parameters on the influence coefficient of axial compression strength  $\eta_N$ . As shown in Figure 13, it reveals that  $\eta_N$  peaks when the number of external ribs  $n$  is 2, followed by  $n = 4$ , and hits its lowest when  $n = 3$ , though the differences are slight. Meanwhile,  $\eta_N$  decreases with the increase of  $\alpha$  and  $c$ . The results of all parameter analyses are illustrated in Figure 14.

## 5.3. Calculation method

In practical engineering, the direction of the bending moment on a joint is unpredictable, leaving the load angle  $\alpha$  indeterminate. Therefore, the lower envelope method is employed for fitting, yielding a



curve that illustrates the correlation between the influence coefficient of axial compression strength  $\eta_N$  and the eccentricity ratio  $c$ .  $\eta_N$  obtained from the experiments also illustrated in Figure 14. Compare the predicted curve for the relationship of  $\eta_N$  and  $c$  to the test results, it demonstrates that the proposed curve gives a conservative prediction. Hence, under the given ranges of parameters  $n \in \{2, 3, 4\}$ ,  $\frac{t_r}{t} \in [0.5, 1.5]$ ,  $\frac{h}{D} \in [0.125, 0.25]$  and  $D \in [300, 900]$  mm, the load-bearing capacity of WHSJ s with external trapezoidal ribs subjected to both axial compression and bending moment could be obtained through Eq. (6), Eq. (8) and Figure 14.

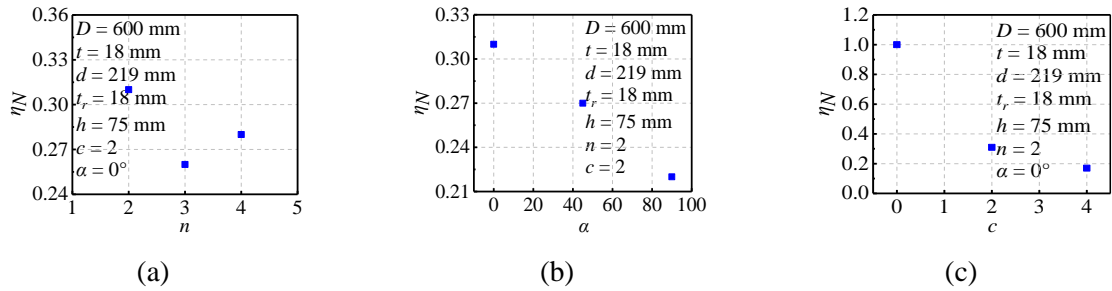


Figure 13:  $\eta_N$  v.s studied parameter: (a)  $n$ ; (b)  $\alpha$ ; (c)  $c$

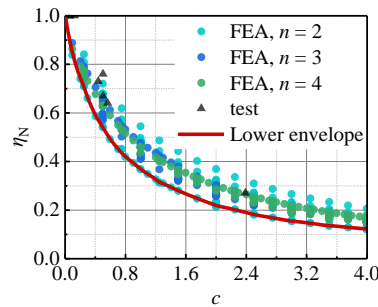


Figure 14: Correlation of  $\eta_N$  and  $c$

## 6. Conclusions

This paper presents an experimental and numerical study on the static performance of WHSJ s with external trapezoidal ribs subjected to both axial compression and bending moment. The conclusions are summarized as follows:

- (1) The experimental results indicates that the specimens failed due to strength loss. Additionally, it is observed that the strength of the specimen decreases with an increase in the load angle and eccentricity.
- (2) The numerical model is developed and calibrated against the experimental results. The deformation the load-displacement responses of the specimens from numerical simulations aligns with those from experiments. Consequently, the developed FE model is capable of simulating the static performance of the reinforced WHSJ s under eccentric compression.
- (3) Parametric studies reveal that  $\eta_N$  decreases with the increase of  $\alpha$  and  $c$ . The lower envelope method is employed to elucidated the correlation of  $\eta_N$  and  $c$ . Thus, the load-bearing capacity of the reinforced WHSJ s under both axial compression and bending moment is established, based on  $\eta_N$ - $c$  correlation and the axial strength of the joints.

## Acknowledgements

This work was supported by the Natural Science Foundation of China (Grant No. 52178175) and a research grant from Center for Balance Architecture of Zhejiang University of China.

## References

- [1] X. Xu, T. Shu, J. Zheng, and Y. Luo, "Experimental and numerical study on compressive behavior of welded hollow spherical joints with external stiffeners," *Journal of Constructional Steel Research*, vol. 188, p. 107034, 2022.
- [2] S. Dong, H. Tang, Y. Zhao, X. Fu, and L. Gu, "Load-carrying capacity and practical calculation method for welded hollow special joints subject to combined axial force and bending moment," *China Civil Engineering Journal*, vol. 38, pp. 21-30, 2005.
- [3] L. Xing, Y. Zhao, S. Dong, L. Gu, and X. Fu, "Finite element analyses and experiments on welded spherical joints with rectangular tubes," *Journal of Zhejiang University (Engineering Science)*, vol. 40, pp. 1559-1563, 2006.
- [4] S. Dong, L. Xing, Y. Zhao, L. Gu, and X. Fu, "Load-carrying capacity and practical calculation method of welded hollow spherical joints connected with square steel tubes," *Journal of Building Structures*, vol. 26, pp. 27-37, 2005.
- [5] Z. Guo, X. Xu, Y. Du, and Z. Chen, "Behaviors of welded hollow spherical joints strengthened by unidirectional annular ribs," *Structures*, vol. 30, pp. 11-24, 2021.
- [6] H. Liu, H. Gao and Z. Chen, "Research on reinforcing method for welded hollow spherical joints," *Journal of Constructional Steel Research*, vol. 182, p. 106685, 2021.
- [7] T. Shu, X. Xu, W. Pan, W. Huang, and Y. Luo, "Compressive performance of welded hollow spherical joints with external triangular ribs," *Engineering Structures*, vol. 280, p. 115717, 2023.
- [8] T. Shu, X. Xu and Y. Luo, "On compressive behavior of large welded hollow spherical joints with both internal and external stiffeners," *Steel and Composite Structures*, vol. 46, pp. 211-220, 2023.
- [9] "China technical specification for space frame structures," *JGJ 7-2010*, Beijing, China: China Architecture & Building Press, 2010.
- [10] "Steel and steel products-location and preparation of samples and test pieces for mechanical testing," *GB/T 2975-2018*, Beijing, China: Standards Press of China, 2018.
- [11] X. Yun and L. Gardner, "Stress-strain curves for hot-rolled steels," *Journal of Constructional Steel Research*, vol. 133, pp. 36-46, 2017.
- [12] "ANSYS 19.0," [Online]. Available: <https://www.ansys.com>. [Accessed: 2024].



## Copyright Declaration

Before publication of your paper in the Proceedings of the IASS Annual Symposium 2024, the Editors and the IASS Secretariat must receive a signed Copyright Declaration. The completed and signed declaration may be uploaded to the EasyChair submission platform or sent as an e-mail attachment to the symposium secretariat (papers@iass2024.org). A scan into a .pdf file of the signed declaration is acceptable in lieu of the signed original. In the case of a contribution by multiple authors, either the corresponding author or an author who has the authority to represent all the other authors should provide his or her address, phone and E-mail and sign the declaration.

Paper Title: Load-bearing capacity of welded hollow sphere joints with trapezoidal ribs under combined axial compression and bending moment

Author(s): Tingting Shu, Xian Xu

Affiliation(s): Department of Civil Engineering, Zhejiang University

Address: 866 Yuhangtang Road, Hangzhou, Zhejiang, China

Phone: +86 17816617296

E-mail: 12112008@zju.edu.cn

---

I hereby license the International Association for Shell and Spatial Structures to publish this work and to use it for all current and future print and electronic issues of the Proceedings of the IASS Annual Symposia. I understand this licence does not restrict any of the authors' future use or reproduction of the contents of this work. I also understand that the first-page footer of the manuscript is to bear the appropriately completed notation:

*Copyright © 2024 by <name(s) of all of the author(s)>  
Published by the International Association for Shell and Spatial Structures (IASS) with permission*

If the contribution contains materials bearing a copyright by others, I further affirm that (1) the authors have secured and retained formal permission to reproduce such materials, and (2) any and all such materials are properly acknowledged by reference citations and/or with credits in the captions of photos/figures/tables.

Printed name: Tingting Shu

Signature: Tingting Shu

Location: Hangzhou, China

Date: 01-07-2024